International Journal of Nanomedicine

Dovepress
open access to scientific and medical research

Open Access Full Text Article

ORIGINAL RESEARCH

Preparation of Zirconium Hydrogen Phosphate Coatings on Sandblasted/Acid-Etched Titanium for Enhancing Its Osteoinductivity and Friction/Corrosion Resistance

Kai Fang*
Yiding Shen*
Kendrick Hii Ru Yie
Zixin Zhou
Lei Cai
Shuyi Wu
Abdullrahman M Al-Bishari
Mohammed A Al-Baadani
Xinkun Shen
Pingping Ma
Jinsong Liu

School and Hospital of Stomatology, Wenzhou Medical University, Wenzhou, 325000, People's Republic of China

*These authors contributed equally to this work

Background: Sandblasted/acid-etched titanium (SLA-Ti) implants are widely used for dental implant restoration in edentulous patients. However, the poor osteoinductivity and the large amount of Ti particles/ions released due to friction or corrosion will affect its long-term success rate.

Purpose: Various zirconium hydrogen phosphate (ZrP) coatings were prepared on SLA-Ti surface to enhance its friction/corrosion resistance and osteoinduction.

Methods: The mixture of $ZrCl_4$ and H_3PO_4 was first coated on SLA-Ti and then calcined at 450°C for 5 min to form ZrP coatings. In addition to a series of physiochemical characterization such as morphology, roughness, wettability, and chemical composition, their capability of anti-friction and anti-corrosion were further evaluated by friction-wear test and by potential scanning. The viability and osteogenic differentiation of MC3T3-E1 cells on different substrates were investigated via MTT, mineralization and PCR assays.

Results: The characterization results showed that there were no significant changes in the morphology, roughness and wettability of ZrP-modified samples (SLA-ZrP0.5 and SLA-ZrP0.7) compared with SLA group. The results of electrochemical corrosion displayed that both SLA-ZrP0.5 and SLA-ZrP0.7 (especially the latter) had better corrosion resistance than SLA in normal saline and serum-containing medium. SLA-ZrP0.7 also exhibited the best friction resistance and great potential to enhance the spreading, proliferation and osteogenic differentiation of MC3T3-E1 cells.

Conclusion: We determined that SLA-ZrP0.7 had excellent comprehensive properties including anti-corrosion, anti-friction and osteoinduction, which made it have a promising clinical application in dental implant restoration.

Keywords: titanium, zirconium hydrogen phosphate, anti-corrosion, anti-friction, osteoinduction

Introduction

Due to their high success rate, titanium (Ti) implants have become widely acknowledged in the treatment of edentulous patients. However, the biological inertness of Ti-based implants can potentially cause the inadequacy of bone-implant integration.[1] This may lead to aseptic loosening of the implants, which ultimately ends in implant failure.[2,3] In addition, the local release of free metal particles/ions, mainly induced by implant-bone tissue friction or body fluid corrosion, is also another important factor that may contribute to the aseptic loosening of implants.[4,5]

Correspondence: Xinkun Shen; Pingping Ma
School and Hospital of Stomatology, Wenzhou Medical University, 268#Xueyuan West Road, Lucheng District, Wenzhou City, 325000, People's Republic of China
Tel +86-577-88066010; +86-577-88066085
Email 20111902015@cqu.edu.cn; ppma2012@sina.com

Received: 8 September 2021
Accepted: 14 December 2021
Published: 22 December 2021

Graphical Abstract

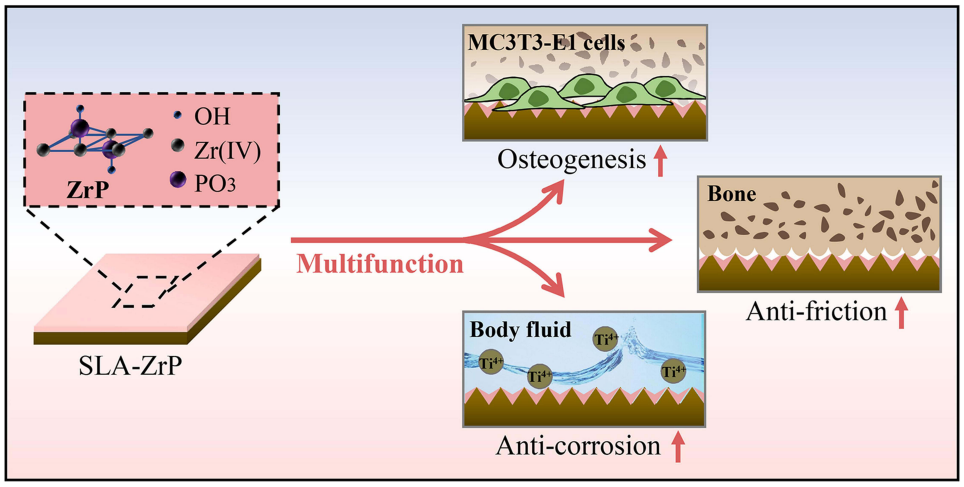

Soto-Alvaredo et al have evaluated the cytotoxicity of both nano-Ti particles (21 nm) and Ti ions in MC3T3-E1 cells.[5] The results suggested that both nano-Ti particles and Ti ions showed obvious cytotoxicity when the concentration was higher than 50 g/mL, with the latter showing early detrimental effects at a concentration of lower than 10 g/mL. Bressan et al further proved that Ti particles/ions would ultimately inhibit new bone formation by promoting reactive oxygen free radical (ROS) expression to induce an oxidative stress (OS) microenvironment.[6] Therefore, it is of great theoretical and clinical significance to enhance the friction/corrosion resistance and biological activity of Ti implants by surface modification for further improving their early osseointegration.

Sandblasting and acid etching (SLA) treatment is one of the most widely utilized implant surface modification techniques. This has been demonstrated to be beneficial for shortening the healing time of Ti-based implants as it provides more attachment area for osteoblast.[7] However, SLA technique in general does not endow Ti-based implants with enhanced corrosion/friction resistance and osteoinduction capabilities. Within the dental implant microenvironment, the inevitable interaction between the metal implants—tissue fluid (consisting of Na^+, organic acids, proteins and so on) and/or saliva (consisting of H_2O, Cl^-, amino acid and so on) may induce metal corrosion by electrochemical oxidation reactions.[8] It has been demonstrated that due to the corrosion behavior, large amounts of Ti particles/ions would be released into surrounding bone tissues. Moreover, compared to successful implant surgery, more Ti particles were detected at peri-implantitis sites, indicating that the level of inflammation was closely related to the corrosion behavior of Ti implants.[9] According to another available report, it was determined that the corrosion resistance of SLA-treated Ti implants is comparable to that of pure Ti.[10] In addition, after implantation, a great number of pathogens would accumulate on the implant surfaces and induce pitting corrosion.[11] Otaibi et al have confirmed that the corrosion resistance of SLA was significantly reduced under the influence of pitting corrosion,[12] which would cause further damage to their mechanical and biological properties.[13] It can be concluded that the corrosion-induced metal ion release could not be simply eliminated and rectified through the general SLA pretreatment.

In terms of friction resistance, Zabala et al found that under the influence of wear and plastic deformation, the surface of SLA implant had a certain wear mass loss with the release of Ti particles.[14] Another study conducted by Eger et al found that the exfoliation of Ti particles from SLA-modified Ti implants could significantly promote M1 polarization of macrophages and stimulate osteoclast formation, thereby impairing the osseointegration between SLA implant and surrounding bone tissues.[15] In contrast, in regard to their mechanical interaction with the bone tissue, SLA implants have been proven to promote substantial osseointegration. With this said, however, the bioactivity and osteoinduction capabilities of the SLA structure are insufficient and still need to be further improved.[16] In recent years, through

continuous research, researchers have found that it is difficult to achieve an ideal and clinically efficient implant simply by improving a single function of the material.[17] Therefore, it is vital to improve the anti-corrosion/friction properties and osteoinduction ability simultaneously for further promoting the long-term success rate of Ti-based implants.

Famed for their biocompatibility and friction/corrosion resistance, zirconium phosphate (ZrP) and its derivatives have been thoroughly investigated for their use in a plethora of fields, such as drug transportation, lubricating grease, and friction/corrosion resistant membranes.[18–20] In biomedicine, Hosseinzadeh et al have developed novel ZrP biocompatible nano-bilayers containing methylene blue, which decreased the cytotoxicity of methylene blue to Hu02 human fibroblast cells.[21] As for friction, the α-ZrP doped grease exhibited a stable, dense and low-shear strength friction-resistant film, which was stronger and more durable than materials doped with molybdenum disulfide (MoS_2) and graphene particles.[22] In regard to anti-corrosion efficiency, Huang et al have successfully prepared a series of ZrP/polyurethane (PU) composite materials and demonstrated that the permeability and corrosion current of ZrP/PU samples with 5.0 wt% α-ZrP significantly lower than those of the PU group.[23]

Although separate studies of SLA-Ti or ZrP coatings as described above are common, the actual effect of ZrP coating on SLA-Ti implant is still unclear. Based on the abovementioned defects of SLA-Ti and advantages of ZrP, we proposed a hypothesis for the first time that suitable ZrP coatings on SLA-treated Ti could effectively improve its osteoinductivity and friction/corrosion resistance. The resulting implants were expected to have better early and/or long-term repair effects. As shown in Figure 1A, different ZrP coatings could be successfully constructed on SLA-Ti substrates by sol-gel and high-temperature calcination techniques. These two issues would be further explored in our study: 1) to prepare and screen the optimal ZrP coating for improving the corrosion and friction resistance of SLA-treated Ti; 2) to further verify the osteoinductive properties of ZrP-coated SLA substrates.

Materials and Methods

Sample Preparation

Commercial Ti pieces were purchased from Northwest Institute for Nonferrous Metal Research (Xi'an, China). Initially, the samples were first sandblasted with 110 μm alumina particles under a pressure of 2 bar for 30 s, and then acid-etched in a solution of 33 wt% H_2SO_4 and 0.1 wt % HF for 15 min. The sandblasted/acid-etched specimens were denoted as SLA. The fabrication process of ZrP coatings (Figure 1A) was conducted in concurrence to the experimental protocols set by Kjellin et al.[24] In brief, the preparation of the coating solution consisting of 125 mL p-xylene, 7.5 mL deionized water, 0.5 g zirconium oxychloride ($ZrCl_4$), 294 μL phosphoric acid (H_3PO_4) and 35 g Pluronic L64 was prepared. Next, the target coatings were produced by adding 50 μL of the coating solution on the surface of SLA substrates, rotated at 2800 rpm for 5 s, and heated at 450°C for 5 min. Due to the presence of 0.5 g $ZrCl_4$ in the initial coating solution, the obtained samples were denoted as SLA-ZrP0.5. The SLA-ZrP0.7 samples were fabricated in a similar manner and components with the exception of the varying $ZrCl_4$ (0.7 g) and H_3PO_4 (412 μL) concentration.

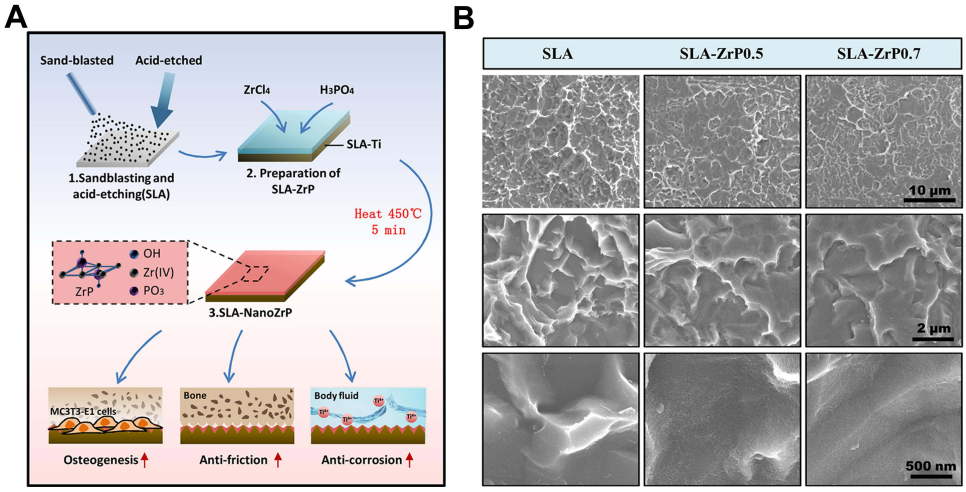

Figure 1 (**A**) Schematic diagram of the experimental procedure; (**B**) representative scanning electron microscopy (SEM) images of SLA, SLA-ZrP0.5 and SLA-ZrP0.7 substrates.

Surface Characterization

The surface morphology and roughness of the samples were characterized by scanning electron microscopy (SEM, Zeiss AURIGA FIB, Germany) and atomic force microscopy (AFM, Dimension, Bruker, Germany). The wettability and crystalline phases were determined by water contact angle (WCA) measuring instrument (DSA30, Kruss, Germany), X-ray diffraction (XRD, D/Max 2500PC, Rigaku, Japan) and grazing incidence X-ray diffraction (GIXRD, Bruker D8, German). The parameters of XRD detection [copper (Cu) kalium (K) Alpha 1 (α1) x-ray] were as follows: the working voltage was 40 kV; the working current was 40 mA; the scanning angle range was 10°–80°; the step length was 0.01°; and the slit was 0.6 mm. Based on the study of Kjellin et al, we estimated that the coating thickness was about 100 nm.[24] Thus, the incident angle was set to 1° and 2° in in GIXRD detection (Cu K α1 x-ray). The scanning angle range and velocity were 5°–90° and 5°/min, respectively. The chemical composition of the coatings was detected by Confocal Raman Microscopy (CRM, inViaQontor, Renishaw, England) and X-ray photoelectron spectroscopy (XPS, Model PHI 5400, Perkin Elmer, USA), respectively. In XPS detection (aluminum K α x-ray), the spot size was 400 microns. Analyser mode was chosen to constant analyzer energy (CAE): the pass energy was 30.0 eV; the energy step size was 0.05 eV; and the number of energy steps was 381. All samples were cleaned at least 3 times with both deionized water and ethanol before taking the above measurements.

Corrosion Test

The corrosion resistances of the different samples were evaluated through potential scanning by an electrochemical workstation (LK2005B, Tianjin Lanlike Chemical and Electron High Technology Co., China). The three-electrode system consisted of saturated calomel electrode (reference electrode), platinum tablet (counter electrode) and relative samples (work electrode). A suitable working area on the surface of the sample was selected for subsequent contact with the electrolyte, while the rest of the surface was insulated with epoxy. The electrolyte used in this work included normal saline and α-Minimum Essential Medium (α-MEM) supplemented with 10% fetal bovine serum (FBS). Before the measurement, the electrolyte was supplied with pure nitrogen enrichment (30 min) to reduce the overall oxygen concentration, which simulated the oral environment.[25] The Tafel curves of different samples were scanned at a rate of 1 mV/s. Corrosion potential (E_{corr}) and corrosion current density (I_{corr}) were finally calculated by using the pre-installed software in the electrochemical workstation.

Friction Test

The friction resistances of the different samples were tested using a friction and wear testing machine (CETR UMT-2, Bruker, USA) at ambient temperature. As shown in Figure 6A, the operation mode was a ball-plane contact type reciprocating friction and the friction mode was a circular reciprocating motion. The specific experimental parameters of the evaluation were listed as follows: the abrasive was alumina ball (φ = 10 mm); the friction test time was 30 min; the load was 2 N; the friction rate was 200 r/min; and the stroke was 10 mm. The coefficient of friction (COF) and the friction force at each point on the motion path were recorded in real time via a connected computer. Through further analysis of the raw data, the surface morphology, wear area/rate, the curves of time-COF, and the average COF could be obtained. Finally, all post-friction test samples were observed under SEM for surface morphology assessment.

Cell Morphology

MC3T3-E1 cells (1×10^4 cells/cm^2) were purchased from Shanghai Institute of Cell Biology and cultured onto different samples in a 24-well plate supplemented with α-MEM medium for 3 d. After fixing by 4% fixative solution (Solarbio Co.) for 30 min and perforating the cell membrane with 0.2% Triton-X solution, the cytoskeleton and nucleus of MC3T3-E1 cells were stained by tetramethylrhodamine phalloidin (Solarbio Co.) and 4′,6-diamidino-2-phenylindole (DAPI, Solarbio Co.) for 40 and 15 min, respectively. Finally, the stained cells were observed by a confocal laser scanning microscope (CLSM, Nikon DS-Ri2, Nikon Instruments Inc., Japan).

Cell Viability

The cell viability of MC3T3-E1 cells was detected by thiazolyl blue tetrazolium bromide (MTT, Solarbio Co.) assay. In brief, MC3T3-E1 cells (1×10^4 cells/cm^2) were cultured in a 24-well plate for 3 and 7 d with α-MEM medium. After that, the α-MEM and MTT solution were added together and incubated at 37°C for 4 h. The mixture solution was then replaced with dimethyl sulfoxide (DMSO) to dissolve the formazan crystals. Finally,

200μL of dissolved solution was collected and detected with a microplate reader (Bio-Rad 680, USA) at 490 nm.

Alizarin Red S Staining

MC3T3-E1 cells (1×10^4 cells/cm^2) were cultured onto the different samples with α-MEM medium for 14 d. The samples were fixed with 200 μL fixation solution (Solarbio Co.) for 15 min and then stained with an Alizarin Red S staining solution (Beyotime Biotechnology Co.) for 40 min. The mineralized nodules on the surface of the specimens were dissolved using cetylpyridinium chloride. Finally, 200 μL of the solution was collected, and the optical density (OD) values were quantified with a microplate reader at 540 nm.

Real-Time qPCR

MC3T3-E1 cells (1×10^4 cells/cm^2) were cultured with α-MEM medium for 7 d. The total RNA was extracted by an RNA simple Total RNA Kit (Tiangen Biotech Co.). According to the manual, first-strand cDNA was prepared using a PrimeScript RT reagent Kit with gDNA Eraser (Takara Bio Inc.). Then, the expression of target genes [runt-related transcription factor 2 (Runx2), alkaline phosphatase (ALP), collagen I (COL I), and osteocalcin (OCN)] was detected with a SYBR Premix EX Taq Kit (Takara Bio Inc.). The relevant primers are listed in Table 1.

Table 1 Real-Time Polymerase Chain Reaction Primers Used in This Study

Target Genes	Primers
Runx2	F: 5′- AGAGTCAGATTACAGATCCCAGG −3′ R: 5′- TGGCTCTTCTTACTGAGAGAGG −3′
ALP	F:5′- GAACAGAACTGATGTGGAATACGAA- 3′ R:5′- CAGTGCGGTTCCAGACATAGTG - 3′
COL I	F:5′- GATGTTGAACTTGTTGTTGCTGAGGG - 3′ R:5′- GGCAGGCGAGATGGCTTATT - 3′
OCN	F:5′- GAACAGACAAGTCCCACACAGC - 3′ R:5′- TCAGCAGAGTGAGCAGAAAGAT - 3′
GAPDH	F:5′- CTCGTCCCGTAGACAAAATGGT - 3′ R:5′- GAGGTCAATGAAGGGGTCGTT - 3′

Statistical Analysis

All data were analyzed by one-way analysis of variance (ANOVA) and Student's *t*-test and expressed as means ± standard deviation. A level of $*p < 0.05$ was considered statistically significant.

Results and Discussion

Surface Characterization

As shown in the SEM images (Figure 1B), a flame-like coating was constructed on the surface of the SLA-treated Ti, in line with a study done by Chiang et al, which proved that the SLA-Ti substrates were successfully fabricated.[26] In the low-resolution images, part of the flame-like structures observed in both the SLA-ZrP0.5 and SLA-ZrP0.7 groups became flat, indicating that the ZrP coating filled the gaps. Furthermore, from the high-resolution images, we could also observe fine strand-like structures appearing on the ZrP-coated substrates. Similar to the results obtained by Kjellin et al, this further proved that the ZrP coatings have adequately filled the gaps in both SLA-ZrP0.5 and SLA-ZrP0.7 groups.[24]

From the AFM images (Figure 2A), we could also discover that the surface morphology of the samples became smoother. The quantified analysis of the average surface roughness (Ra) and root-mean-square roughness (Rq) did not show a significant decrease with the increased amount of ZrP. The detailed roughness values were listed as follows: Ra 0.5 ± 0.05 μm, Rq 0.6 ± 0.06 μm (SLA); Ra 0.5 ± 0.06 μm, Rq 0.6 ± 0.07 μm (SLA-ZrP0.5); and Ra 0.4 ± 0.04 μm, Rq 0.6 ± 0.05 μm (SLA-ZrP0.7).

From Figure 2B, it was found that the WCA of both SLA-ZrP0.5 and SLA-ZrP0.7 were significantly smaller ($p < 0.05$) than that of SLA group. The WCA of SLA-ZrP0.7 was slightly higher than that of SLA-ZrP0.5 but not significant. By the quantitative analysis, the detailed WCA values at 1, 5 and 10 s were listed as follows: 84.7°, 74.4°, 73.1° (SLA); 36.1°, 26.3°, 25.8° (SLA-ZrP0.5); and 39.2°, 34.1°, 33.5° (SLA-ZrP0.7). The hydrophilicity of the ZrP coatings might be attributed to the presence of hydrogen bond interactions between H_2O and hydroxyl group of the ZrP compound.[27]

To investigate the crystalline structures of the different samples, XRD and GIXRD analyses were carried out. In the SLA group, the XRD result (Figure 3A) exhibited the characteristic peaks of Ti (JCPDS 05–0682) and TiH_2 (JCPDS 09–0371), which was consistent with our previous study.[28] The formation of TiH_2 was due to the chemical reaction between hydrogen ion and Ti in the process of acid etching. After the samples were subjected to heating at 450°C for 5 min, the TiH_2 compound disappeared and only the peaks of Ti were detected on the surfaces of both SLA-ZrP0.5 and SLA-ZrP0.7 specimens. A previous study

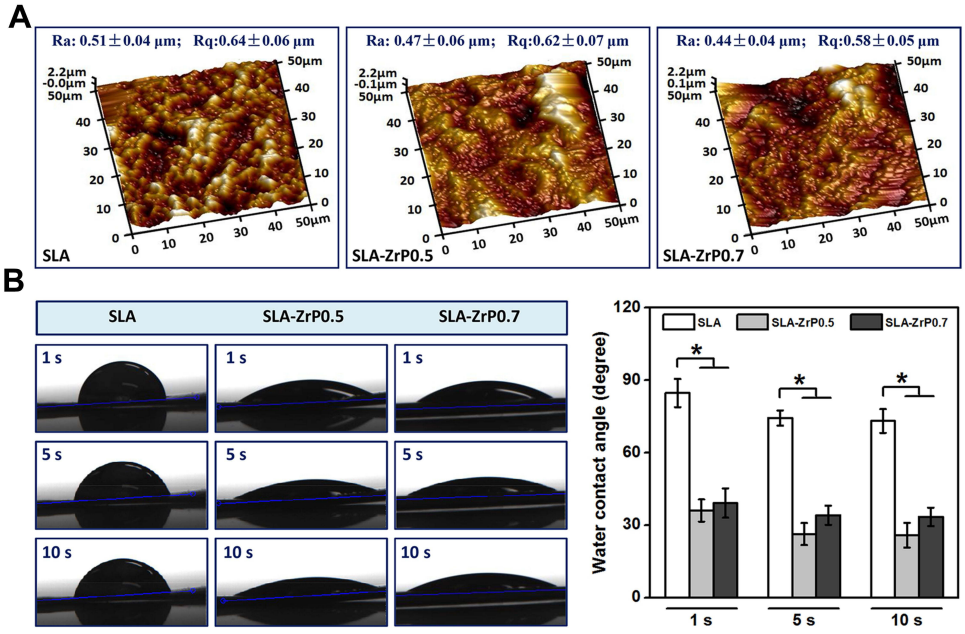

Figure 2 (**A**) Atomic force microscopy (AFM) images and quantified surface roughness [average surface roughness (Ra) and root-mean-square roughness (Rq)] of the different samples; (**B**) representative water contact angle (WCA) images and quantified values of the different samples at 1, 5 and 10 s. Error bars represent mean ± SD for n = 6, *$p < 0.05$.

also discovered that TiH_2 would be decomposed and oxidized into TiO_2 at 300–500°C.[29] Similar to the XRD results, GIXRD with the incident angles of 1 and 2 degrees also showed that there were no ZrP characteristic peaks (Figure S2). According to previous studies, the researchers prepared stripped ZrP with surfactant and also found no ZrP peaks in their XRD patterns.[30,31] Due to the exfoliation effect, ZrP was likely to transform into an amorphous state, which led to the disappearance of the ZrP characteristic peaks. Similarly, in this study, the existence of Pluronic L64 in the calcination process might affect the crystallization of ZrP, possibly causing the absence of ZrP characteristic peaks in the XRD and GIXRD results. Moreover, we also observed a characteristic peak (~13.6°, JCPDS 46–1237) of TiO_2 as a result of 1-degree incidence angle, which may be due to the natural oxidation of the surface after etching.

The Raman spectra of SLA, SLA-ZrP0.5 and SLA-ZrP0.7 are presented in Figure 3B. Only the peaks at 629.7 and 706.9 cm^{-1} were observed in SLA group, which were identified as the characteristic band of TiH_2 according to a previous study.[32] However, in SLA-ZrP0.5 and SLA-ZrP0.7 groups, the characteristic peaks of TiH_2 disappeared, while other peaks at 1067.2, 1392.4 and 1592.8 cm^{-1} appeared. The appearance and disappearance of TiH_2 was caused by the acid-etching and heating treatments, which

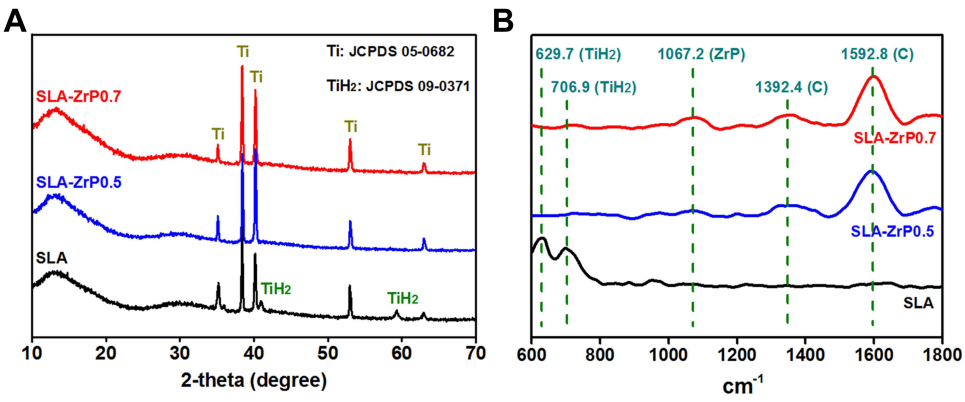

Figure 3 (**A**) X-ray diffraction (XRD) patterns and (**B**) Raman spectrum of SLA, SLA-ZrP0.5 and SLA-ZrP0.7 substrates.

had been confirmed by XRD result (Figure 3A). An in-depth analysis could determine that the small peak at 1067.2 cm^{-1}, the frequency of the antisymmetric ν3 (PO_4) stretching banda,[33] was the characteristic of ZrP, proving that ZrP coating was successfully prepared on the SLA substrates. According to previous studies, the Raman peaks of amorphous substances are usually wider and lower in general compared to crystallized structures.[34,35] Identically, the presence of Pluronic L64 in the initial coating solution could result in the formation of amorphous ZrP, which was why there was only a small ZrP peak in this study. In addition, both in SLA-ZrP0.5 and SLA-ZrP0.7, the Raman spectra also showed peaks in 1392.4 and 1592.8 cm^{-1}, which were D and G bands of the C element. The simultaneous appearance of both D and G bands represents the production of amorphous carbon.[36] This suggested the presence of amorphous carbon on the surfaces of SLA-ZrP0.5 and SLA-ZrP0.7, which was consistent with the finding of C element in the result of XPS (Figures 4A and S1). In addition, it has been proved that amorphous carbon materials could be obtained by calcining carbon sources consisting of C, H and O.[37,38] Based on this, we believed that the organic surfactant (Pluronic L64) resulted in the formation of amorphous carbon after calcination.

To investigate the chemical composition of the surface coating, all samples were evaluated using XPS, and the results are displayed in Figure 4. Firstly, from Figure 4A, we could observe a gradual decrease in Ti element and an increase in Zr and P elements corresponding with the rising amount of initial $ZrCl_4$ and H_3PO_4. In SLA-ZrP0.7 group, the contents of Zr and P were 2.9 at% and 4.8 at%, which were higher than that of SLA-ZrP0.5 (2.2 at% and 3.7 at%). The fitting spectrum (Figure 4B) showed that the Zr3d peak composed of a large amount of ZrP and a small amount of ZrO_2,[39] both of which were increased in the SLA-ZrP0.7 group than in the SLA-ZrP0.5. The P element (P2p3/2 and P2p1/2) in the SLA-ZrP0.7 group was also significantly augmented, in line with the ZrP enhancement in Zr3d (Figure S1). Further investigations of Zr3d and P2p showed that the ratio of Zr/P remained around 60%, and the ratio of ZrP to ZrO_2 was approximately 9:1. A previous study has confirmed that $ZrCl_4$ was easily hydrolyzed in aqueous environment, forming $ZrOCl_2$ and HCl.[40] The $ZrOCl_2$ could further react with H_3PO_4 to form ZrP precipitates.[41] According to another research by Sarkar et al, $ZrOCl_2$ would decompose into amorphous ZrO_2 powder when subjected to high temperature (> 200°C),[42] which resulted in the formation of a small amount of ZrO_2 in the target ZrP

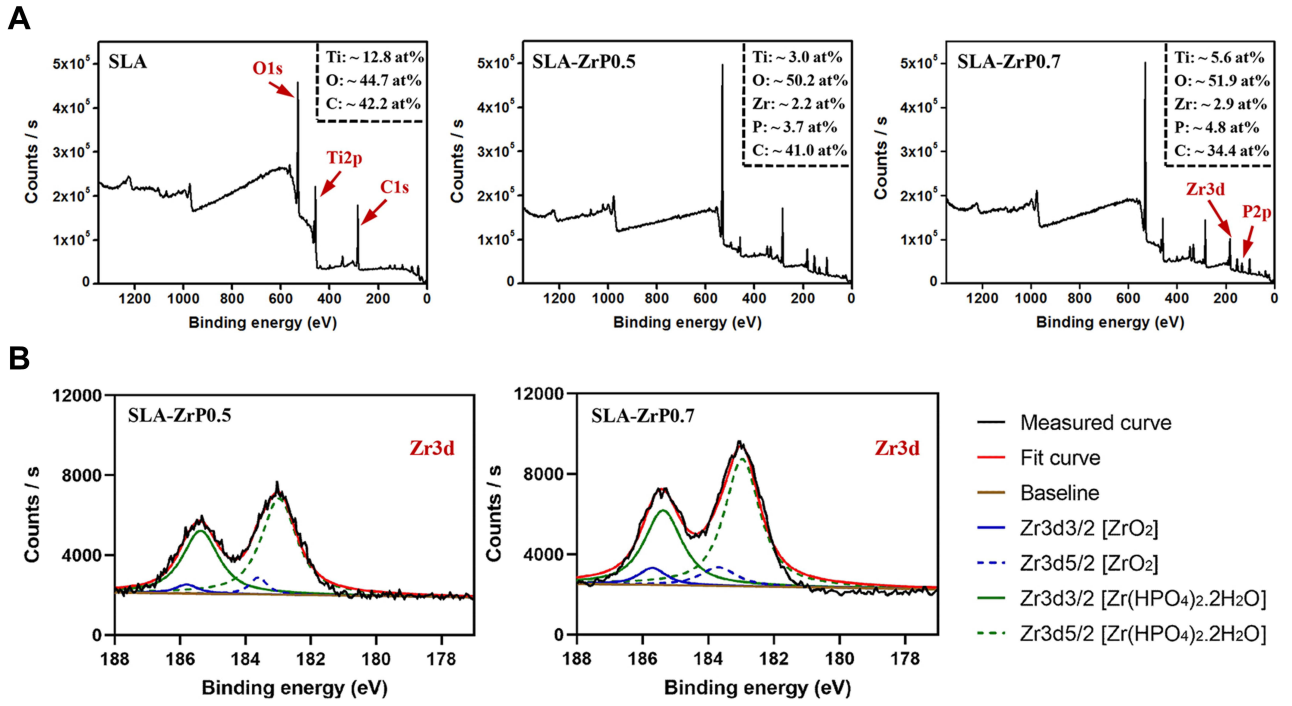

Figure 4 (**A**) X-ray photoelectron spectroscopy (XPS) patterns and element contents of SLA, SLA-ZrP0.5 and SLA-ZrP0.7 samples; (**B**) split-fitting spectra of the Zr3d peaks in different groups.

coatings. The presence of ZrP and ZrO_2 in the coatings was also confirmed by the fitting spectrum of O1s (Figure S1). Moreover, the fitting results (Figure S1) further displayed that C1s could be decomposed into amorphous carbon, C=C, and C-OH in both SLA-ZrP0.5 and SLA-ZrP0.7. Previous study has revealed that the peaks of amorphous carbon and C=C were associated with the hybridization of carbon sp2,[43] which were also closely related to the appearance of D and G bands in the resulting Raman (Figure 3B). The C-OH in samples might be caused by environmental contamination.[44]

Corrosion Resistance of Different Samples

To investigate the corrosion resistance of the different coatings, we performed a linear scan of SLA, SLA-ZrP0.5 and SLA-ZrP0.7 immersed in saline and FBS-supplemented α-MEM medium. The polarization curves are depicted in Figure 5A and B. In saline solution and α-MEM medium, the polarization curves of SLA, SLA-ZrP0.5 and SLA-ZrP0.7 were basically similar. It was easy to discover that E_{corr} increased with the increase of ZrP. Based on Tafel extrapolation, we further analyzed the typical electrochemical parameters of the polarization curves via electrochemical software (Figure 5C and D), including E_{corr} and I_{corr}. The E_{corr} of SLA-ZrP0.5 and SLA-ZrP0.7 were −0.03 and 0.01 V in saline solution, which was significantly better ($p < 0.05$) than that of SLA (−0.2 V). In α-MEM medium, the E_{corr} of SLA-ZrP0.5 and SLA-ZrP0.7 was also slightly higher than that of SLA group (−0.7 V). In addition, the I_{corr} of SLA-ZrP0.5 and SLA-ZrP0.7 were 0.1 (in saline solution)/1.2 (in α-MEM medium) and 0.1 (in saline solution)/0.8 (in α-MEM medium) lg(i)μA/cm^2, which was significantly lower ($p < 0.05$) than that of SLA [0.4/1.7 lg(i)μA/cm^2]. Consequently, not only in saline solution but also in FBS-supplemented α-MEM medium, SLA-ZrP0.7 substrates had the highest E_{corr} and the lowest I_{corr}, which proved its excellent corrosion resistance.

Localized corrosion has been confirmed to occur through galvanic interactions when the entire metal implant surface is exposed to bodily fluids, which include general corrosion, pitting corrosion, and electrochemical/mechanical processes.[8] The 10% FBS-supplemented α-MEM medium used in this study was rich in L-Glutamine, albumin and so on. Previous research has shown that the corrosion rate of commercially pure Ti in cell medium was 31% higher than that in normal saline.[45] Further studies demonstrated that albumin played a key

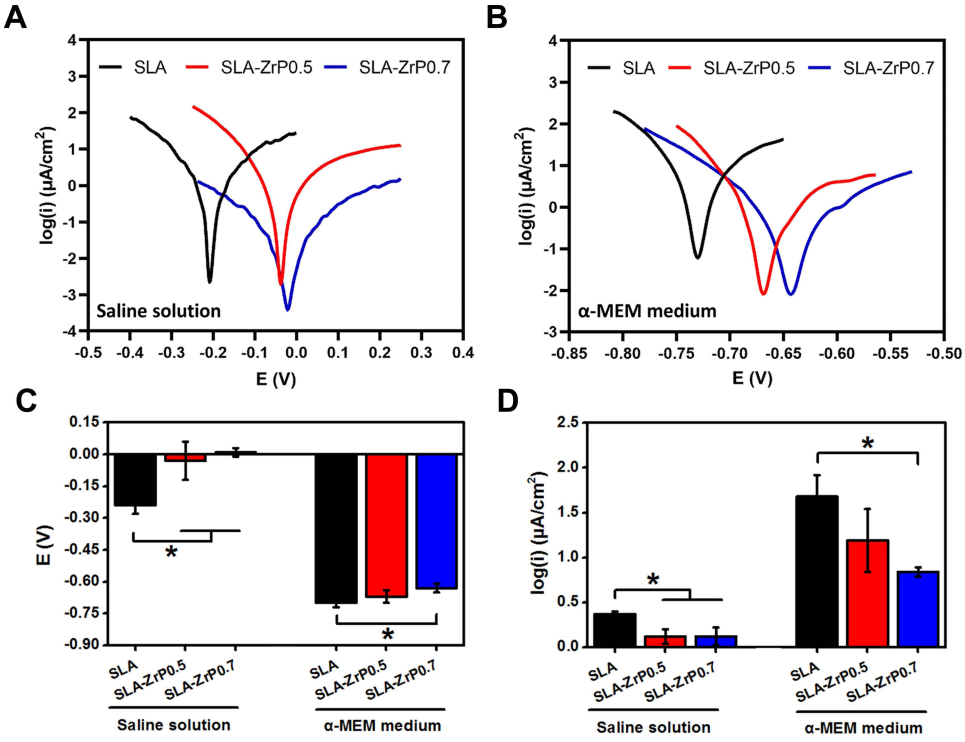

Figure 5 The Tafel curves of the different samples measured in saline solution (**A**) and α-MEM (**B**); quantified corrosion potential (**C**) and corrosion current density (**D**) of the different samples in saline solution and α-MEM. Error bars represent mean ± SD for n = 6, *$p < 0.05$.

role in increasing the rate of electrochemical corrosion, which might be due to the fact that albumin with an isoelectric point of 4.5 remained negatively charged in normal cell culture medium (~ pH 7.4).[45,46] Moreover, parts of the proteins could react with the metal to form stable complex compounds, which also led to the increase in the corrosion velocity.[46] Therefore, we observed a significant decrease and increase in the E_{corr} and I_{corr} values for the samples immersed in the FBS-supplemented α-MEM medium when compared with the saline groups.

Friction Resistance of Different Samples

As a result of layered structure and the slide inclination between adjacent sheets under shear function, ZrP coatings have excellent performance on lubrication.[47] The images shown in Figure 6A depict the surface morphology and abrasion area on the sample after friction-wear testing. There was a similar abrasion profile on both sides of the samples caused by the clamping of the samples. According to the label on the left side of the image, a change in color from red to black indicates a gradual increase in the amount of surface wear. In the SLA group, a large dark green area of wear was present in the center of the sample. In the SLA-ZrP0.7 group, the black-green color representing the abrasion area was substantially reduced with the sample surface only presenting bright green color. Further SEM observations (Figure S3A) showed deep grinding grooves on the SLA surface resulting in difficulties in observing their original structures. In contrast, a large number of ridge structures remained in the wear area on the SLA-ZrP0.5 and SLA-ZrP0.7 samples. Next, the abrasion area and wear rate of each group were quantified and displayed in Figures S3B and 6B, respectively. It was clear that the abrasion area of SLA-ZrP0.5 (10,402.9 ± 144.1 μm^2) and SLA-ZrP0.7 (9805.1 ± 193.0 μm^2) were significantly lower ($p < 0.05$) than that of the SLA (36017.0 ± 1360.1 μm^2). The wear rate also showed a similar decreasing trend: SLA-ZrP0.7 (2.1 ± 0.04 mm^3/s) ≈ SLA-ZrP0.5 (2.2 ± 0.03 mm^3/s) < SLA (7.5 ± 0.3 mm^3/s). In addition, the time–COF curves (Figure S3C) displayed that each group had a continuous upward trend around 0–180 s and then tended to stabilize or slightly increase. The initial trend of irregular growth may be related to the friction adaptation period.[48] It was also observed that the COF value of SLA was slightly higher than other two groups during the stable period. And as shown as Figure 6C, the average COF of SLA (0.7 ± 0.04) was slightly higher than SLA-ZrP0.5 (0.6 ± 0.02) and SLA-ZrP0.7 (0.6 ± 0.03). To sum up, these results indicated that ZrP coatings significantly enhanced the ability of anti-friction.

It has been claimed that the surface roughness of materials was closely related to their COF and that an increase in the surface roughness would increase the COF and friction

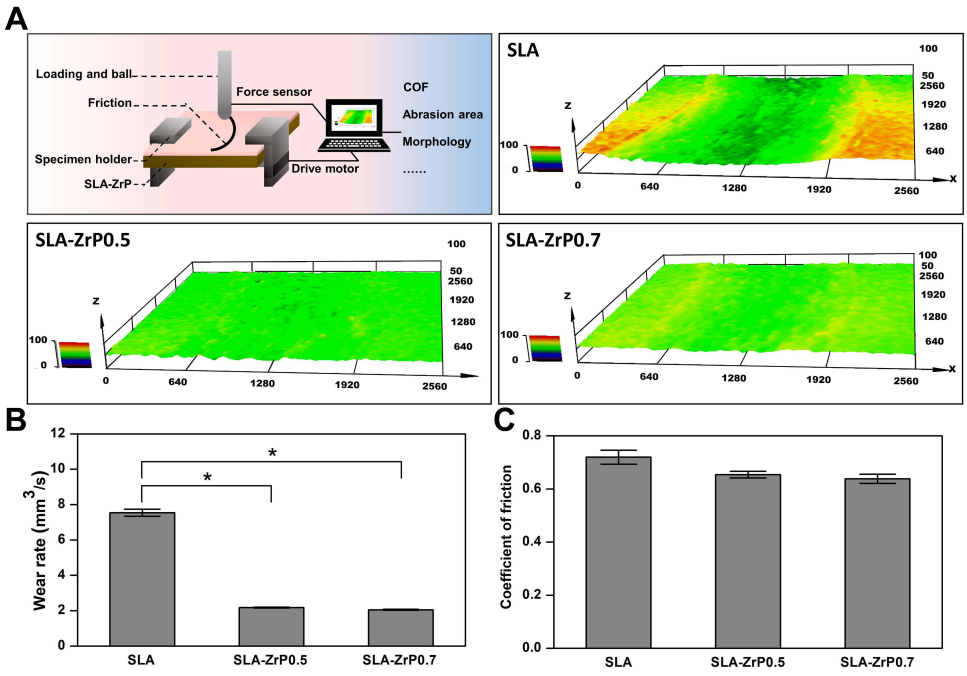

Figure 6 (**A**) Schematic diagram of the UMT-3 friction resistance test and surface morphology of the different samples after analysis; quantified wear rate (**B**) and coefficient of friction (**C**) in different groups. Error bars represent mean ± SD for n = 6, *$p < 0.05$.

force.[49] Although a smooth RP coating has been successfully prepared on the SLA surface herein, we found that the surface roughness mainly depended on the flame-like microstructure. This would explain why there was a similar and non-significantly different COF trend among the groups. Through in-depth analyses, we also discovered substantial changes to the cross-sectional area and wear rate due to the ZrP coatings, which played an important role in improving the tribological properties of SLA samples. As a typical layered nanomaterial, ZrP has been confirmed to have a covalent network structure formed by ZrO_6 sheets and tetrahedral HPO_4^{2-} through Van der Waals forces.[50,51] At the molecular level, the interaction between the adjacent layers played a key role in the friction behavior and resistance of nanoparticles.[52] Therefore, under shearing conditions, layered materials are more prone to result in intergranular slippage, leading to an increased friction resistance.[53] In addition, ZrP, a widely applied nanolubricant additive, could repair scars and grooves of a material surface via surface repairing and polishing effect, which in turn could considerably enhance friction resistance.[54,55] Another study claimed that after doping ZrP nanosheets in polyvinyl alcohol, its nano-mechanical properties, such as hardness and elastic modulus, were improved.[56] Therefore, we believed that although the ZrP coating did not effectively change the COF of SLA, its layered structures and superior hardness/elastic modulus would play a direct role in the wear process, resulting in a significant decrease in wear area and wear rate.[54–57]

Effects of Different Samples on MC3T3-E1 Cells

To investigate the different effects of ZrP coating on osteogenesis, a series of in vitro cellular experiments were carried out. From the CLSM images (Figure 7A), we could see that the fluorescence intensity and the number of MC3T3-E1 cells were similar for every group. However, the cell spreading area increased slightly with the increase of ZrP.

As for the cell viability, the MTT result (Figure 7B) of MC3T3-E1 cells showed that both SLA-ZrP0.5 and SLA-ZrP0.7 significantly ($p < 0.05$) promoted the cell viability when compared with the SLA group after 3 and 7 d. Similar to the MTT result, the cells on the surface of ZrP-modified samples also showed a significant increase ($p < 0.05$) in mineralization level (Figure 7C): SLA-ZrP0.5 and SLA-ZrP0.7 groups were about 112% and 115%, respectively. In addition, when compared to the SLA and SLA-ZrP0.5 groups at the molecular level, the SLA-ZrP0.7 samples exhibited a significantly ($p < 0.05$) enhanced expression of Runx2, ALP, COL I and OCN genes (Figure 8). It was also found that the expression of Col I and Runx2 genes in the SLA-ZrP0.5 group were higher ($p < 0.05$) than that of the SLA group, while the expression of ALP and OCN genes had no significant differences between the two groups.

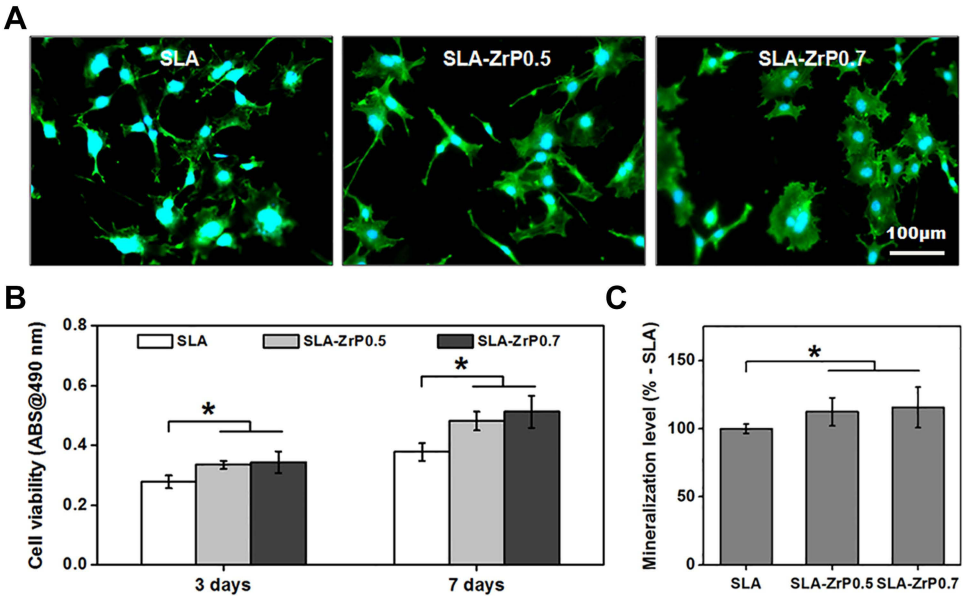

Figure 7 (**A**) Representative fluorescent staining images of cell morphology in the different groups; (**B**) cell viability of MC3T3-E1 cells on the different samples after 3 and 7 d; (**C**) mineralization level of MC3T3-E1 cells on the different substrates after 14 d. Error bars represent mean ± SD for n = 6, *$p < 0.05$.

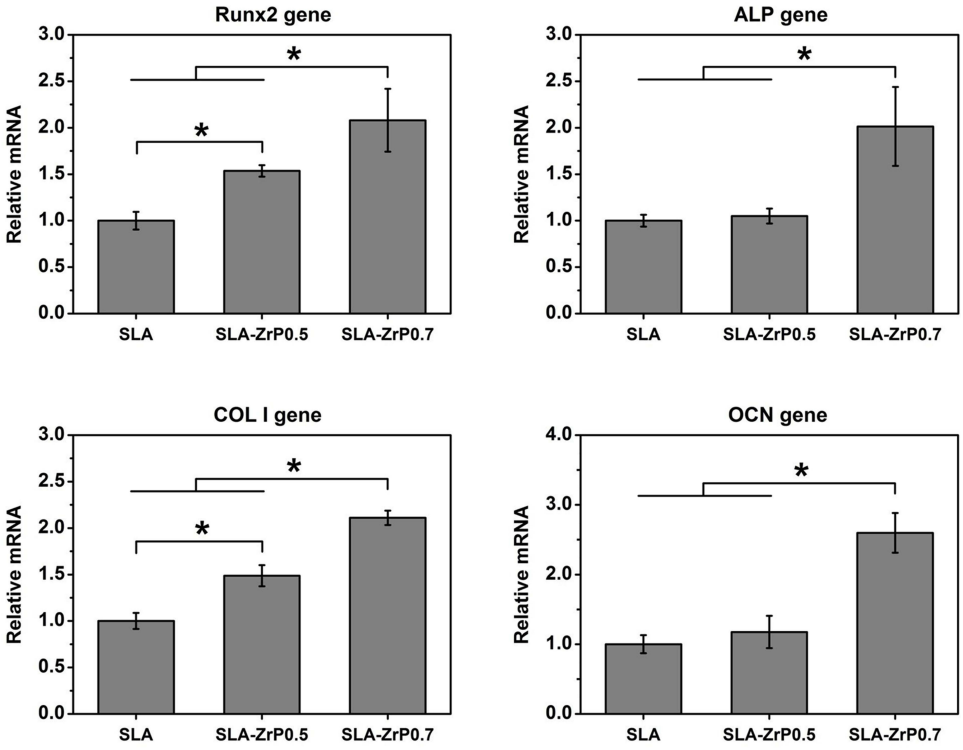

Figure 8 Relative expressions of Runx2, ALP, COL I and OCN genes of MC3T3-E1 cells on the different substrates after 14 d. Error bars represent mean ± SD for n = 6, *$p < 0.05$.

In summation, the ZrP coating increased the spreading area and viability of MC3T3-E1 cells, which might be attributable to the ZrP structure on the surface of the SLA substrate.[58,59] Moreover, we have proven that the ZrP coating could significantly augment the osteoinduction capacity by enhancing the mineralization level through up-regulating the expressions of osteogenesis-related genes (Runx2, ALP, COL I & OCN). In general, SLA-ZrP not only had good cytocompatibility but also had good osteoinductive potential, which was of great significance for its clinical application and service life.

Conclusion

In this study, ZrP coatings were successfully prepared on the SLA-treated Ti substrates by sol-gel and high-temperature calcination techniques. Through the evaluation of the chemical composition of both SLA-ZrP0.5 and SLA-ZrP0.7 coatings, we found that the ZrP compound (including a small amount of ZrO_2) was formed after heat treatment. Although the corrosion resistance of each group in α-MEM medium supplemented with FBS was obviously lower than that in saline solution, SLA-ZrP0.5 and SLA-ZrP0.7 (especially the latter) displayed better performance on E_{corr} and I_{corr} in both electrolytes compared with SLA group. Besides, SLA-ZrP0.7 also showed the best friction resistance and osteoinductive potential. In conclusion, this novel multifunctional Ti-based implant has excellent osteoinduction, anti-corrosion, and anti-friction properties, which exhibits a promising potential in implant application.

Acknowledgments

This work was funded by Zhejiang Provincial Science and Technology Project for Public Welfare (LY21H180006 and LGF21H140004), National Natural Science Foundation of China (82171004, 82071170 and 81870810), Key Technological Innovation Projects of Wenzhou (ZY2019009), Wenzhou Public Welfare Science and Technology Project (Y20190099), Wenzhou Medical University Basic Scientific Research Operating Expenses (KYYW201905).

Disclosure

The authors report no conflicts of interest in this work.

References

1. Nie B, Ao H, Zhou J, Tang T, Yue B. Biofunctionalization of titanium with bacitracin immobilization shows potential for anti-bacteria, osteogenesis and reduction of macrophage inflammation. *Colloids Surf B Biointerfaces*. 2016;145:728–739.

2. De Angelis F, Papi P, Mencio F, Rosella D, Di Carlo S, Pompa G. Implant survival and success rates in patients with risk factors: results from a long-term retrospective study with a 10 to 18 years follow-up. *Eur Rev Med Pharmacol Sci*. 2017;21:433–437.
3. Ray S, Thormann U, Eichelroth M, et al. Strontium and bisphosphonate coated iron foam scaffolds for osteoporotic fracture defect healing. *Biomaterials*. 2018;157:1–16.
4. Balachandran S, Zachariah Z, Fischer A, et al. Atomic scale origin of metal ion release from hip implant taper junctions. *Adv Sci*. 2018;7:1903008.
5. Soto-Alvaredo J, Blanco E, Bettmer J, et al. Evaluation of the biological effect of Ti generated debris from metal implants: ions and nanoparticles. *Metallomics*. 2014;6:1702–1708.
6. Bressan E, Ferroni L, Gardin C, et al. Metal nanoparticles released from dental implant surfaces: potential contribution to chronic inflammation and peri-implant bone loss. *Materials (Basel)*. 2019;12(12):2036.
7. Feng F, Wu Y, Xin H, et al. Surface characteristics and biocompatibility of ultrafine-grain Ti after sandblasting and acid etching for dental implants. *ACS Biomater Sci Eng*. 2019;5:5107–5115.
8. Asri RIM, Harun WSW, Samykano M, et al. Corrosion and surface modification on biocompatible metals: a review. *Mater Sci Eng C Mater Biol Appl*. 2017;77:1261–1274.
9. Suárez-López Del Amo F, Garaicoa-Pazmiño C, Fretwurst T, Castilho RM, Squarize CH. Dental implants-associated release of titanium particles: a systematic review. *Clin Oral Implants Res*. 2018;29:1085–1100.
10. Zhang E, Liu C. Effect of surface treatments on the surface morphology, corrosion property, and antibacterial property of Ti-10Cu sintered alloy. *Biomed Mater*. 2015;10:045009.
11. Zhou W, Peng X, Zhou X, Li M, Ren B, Cheng L. Influence of bioaging on corrosion behavior of different implant materials. *Clin Implant Dent Relat Res*. 2019;21:1–10.
12. Otaibi AA, Sherif EM, Allnlfaiy MQ, Zinelis S, Jabbari Y. Corrosion resistance of coupled sandblasted, large-grit, acid-etched (SLA) and anodized Ti implant surfaces in synthetic saliva. *Clin Exp Dental Res*. 2019;5:452–459.
13. Souza JC, Henriques M, Oliveira R, Teughels W, Celis JP, Rocha LA. Do oral biofilms influence the wear and corrosion behavior of titanium? *Biofouling*. 2010;26:471–478.
14. Zabala A, Blunt L, Tejero R, Llavori I, Tato W. Quantification of dental implant surface wear and topographical modification generated during insertion. *Surf Topography: Metrol Prop*. 2019;8:0 15002.
15. Eger M, Hiram-Bab S, Liron T, Sterer N, Carmi Y, Kohavi D. Mechanism and prevention of titanium particle-induced inflammation and osteolysis. *Front Immunol*. 2018;9:2963.
16. Jang TS, Jung HD, Kim S, et al. Multiscale porous titanium surfaces via a two-step etching process for improved mechanical and biological performance. *Biomed Mater*. 2017;12:025008.
17. He W, Yin X, Xie L, et al. Enhancing osseointegration of titanium implants through large-grit sandblasting combined with micro-arc oxidation surface modification. *J Mater Sci Mater Med*. 2019;30:73.
18. Cámara-Torres M, Duarte S, Sinha R, et al. 3D additive manufactured composite scaffolds with antibiotic-loaded lamellar fillers for bone infection prevention and tissue regeneration. *Bioact Mater*. 2020;6:1073–1082.
19. Xiao HP, Wei D, Kan YW, Clearfield A, Liang H. Amine-intercalated α-zirconium phosphates as lubricant additives. *Appl Surf Sci*. 2015;329:384–389.
20. Sigwadi R, Dhlamini MS, Mokrani T, Ṇemavhola F, Nonjola PF, Msomi PF. The proton conductivity and mechanical properties of Nafion®/ZrP nanocomposite membrane. *Heliyon*. 2019;5:e02240.
21. Hosseinzadeh R, Khorsandi K. Photodynamic effect of Zirconium phosphate biocompatible nano-bilayers containing methylene blue on cancer and normal cells. *Sci Rep*. 2019;9:14899.
22. Dai Y, Niu W, Zhang X, Xu H, Dong J. Tribological investigation of layered zirconium phosphate in anhydrous calcium grease. *Lubricants*. 2017;5:22.
23. Huang TC, Lai GH, Li CE, et al. Advanced anti-corrosion coatings prepared from α-zirconium phosphate/polyurethane nanocomposites. *RSC Adv*. 2017;7:9908–9913.
24. Kjellin P, Vikingsson L, Danielsson K, Johansson P, Wennerberg A. A nanosized zirconium phosphate coating for peek implants and its effect in vivo. *Materialia*. 2020;10:100645.
25. Díaz I, Pacha-Olivenza Á, Tejero R, et al. Corrosion behavior of surface modifications on titanium dental implant. In situ bacteria monitoring by electrochemical techniques. *J Biomed Mater Res B Appl Biomater*. 2018;106:997–1009.
26. Chiang HJ, Hsu HJ, Peng PW, et al. Early bone response to machined, sandblasting acid etching (SLA) and novel surface-functionalization (SLAffinity) titanium implants: characterization, biomechanical analysis and histological evaluation in pigs. *J Biomed Mater Res A*. 2016;104:397–405.
27. Ibrahim Y, Abdulkarem E, Naddeo V, Banat F, Hasan SW. Synthesis of super hydrophilic cellulose-alpha zirconium phosphate ion exchange membrane via surface coating for the removal of heavy metals from wastewater. *Sci Total Environ*. 2019;690:167–180.
28. Shen X, Ma P, Hu Y, Xu G, Zhou J, Cai K. Mesenchymal stem cell growth behavior on micro/nano hierarchical surfaces of titanium substrates. *Colloids Surf B Biointerfaces*. 2015;127:221–232.
29. David RB, Finkelstein Y, Grinberg E, Samuha S, Cohen D. Oxidation induced cubic-tetragonal phase transformation in titanium hydride powders. *Int J Hydrogen Energy*. 2020;45:25043–25053.
30. Zhao M, Baker J, Jiang Z, et al. Preparation of well-exfoliated poly (ethylene-co-vinyl acetate)/α-zirconium phosphate nanocomposites. *Langmuir*. 2021;37:4550–4561.
31. Wang L, Xu WH, Yang R, et al. Electrochemical and density functional theory investigation on high selectivity and sensitivity of exfoliated nano-zirconium phosphate toward lead (II). *Anal Chem*. 2013;85:3984–3990.
32. Ali N, Bashirc S, Umm-i-Kalsoom BN, Rafique MS, Husinsky W. Effect of liquid environment on the titanium surface modification by laser ablation. *Appl Surf Sci*. 2017;405:298–307.
33. Bhatt R, Rathod VA, Rathod SB, Padmaja P. Self-assembled chitosan-zirconium phosphate nanostructures for adsorption of chromium and degradation of dyes. *Carbohydr Polym*. 2019;208:441–450.
34. Katsikini M, Proiou E, Vouroutzis N, et al. Crystalline and amorphous calcium carbonate as structural components of the Calappa granulata exoskeleton. *J Struct Biol*. 2020;211:107557.
35. Liu W, Liu Y, Huang J, et al. Identification and investigation of the vibrational properties of crystalline and co-amorphous drugs with Raman and terahertz spectroscopy. *Biomed Opt Express*. 2019;10:4290–4304.
36. Khanam A, Tripathi SK, Roy D, Nasim M. A facile and novel synthetic method for the preparation of hydroxyl capped fluorescent carbon nanoparticles. *Colloids Surf B Biointerfaces*. 2013;102:63–69.
37. Elizalde-González MP, García-Díaz E, Sabinas-Hernández SA. Novel preparation of carbon-TiO_2 composites. *J Hazard Mater*. 2013;263(Pt 1):73–83.
38. Escamilla-Pérez AM, Louvain N, Boury B, Brun N, Mutin PH. Ethers as oxygen donor and carbon source in non-hydrolytic sol-gel: one-pot, atom-economic synthesis of mesoporous TiO_2--carbon nanocomposites. *Chemistry*. 2018;24:4982–4990.
39. Aleksei O, Alina S, Anton M, Se Ba Stian B, Sabine W, Egor K. Oxidation behavior of Zr–1Nb corroded in air at 400 °C after plasma immersion titanium implantation. *Metals Open Access Metallurgy J*. 2018;8(1):27.
40. Taddei M, van Bokhoven JA, Ranocchiari M. Influence of water in the synthesis of the zirconium-based metal-organic framework UiO-66: isolation and reactivity of $[ZrCl(OH)_2(DMF)_2]Cl$. *Inorg Chem*. 2020;59:7860–7868.

41. Cheng Y, Wang XT, Jaenicke S, Chuah GK. Minimalistic liquid-assisted route to highly crystalline α-zirconium phosphate. *Chem Sus Chem*. 2017;10:3235–3242.
42. Sarkar D, Swain SK, Adhikari S, Reddy BS, Maiti HS. Synthesis, mechanical properties and bioactivity of nanostructured zirconia. *Mater Sci Eng C Mater Biol Appl*. 2013;33:3413–3417.
43. Zielinski W, Kamedulski P, Smolarkiewicz-Wyczachowski A, Skorupska M, Lukaszewicz JP, Ilnicka A. Synthesis of hybrid carbon materials consisting of N-doped microporous carbon and amorphous carbon nanotubes. *Materials (Basel)*. 2020;13(13):2997.
44. Wennerberg A, Jimbo R, Stübinger S, Obrecht M, Dard M, Berner S. Nanostructures and hydrophilicity influence osseointegration: a biomechanical study in the rabbit tibia. *Clin Oral Implants Res*. 2014;25:1041–1050.
45. Williams RL, Brown SA, Merritt K. Electrochemical studies on the influence of proteins on the corrosion of implant alloys. *Biomaterials*. 1988;9:181–186.
46. Ehrensberger MT, Gilbert JL. The effect of static applied potential on the 24-hour impedance behavior of commercially pure titanium in simulated biological conditions. *J Biomed Mater Res B Appl Biomater*. 2010;93:106–112.
47. Xiao H, Liu S. Zirconium phosphate (ZrP)-based functional materials: synthesis, properties and applications. *Mater Des*. 2018;155:19–35.
48. Krbata M, Eckert M, Bartosova L, et al. Dry sliding friction of tool steels and their comparison of wear in contact with ZrO_2 and X46Cr13. *Materials (Basel)*. 2020;13(10):2359.
49. Cury SE, Aliaga-Del Castillo A, Pinzan A, Sakoda KL, Bellini-Pereira SA, Janson G. Orthodontic brackets friction changes after clinical use: a systematic review. *J Clin Exp Dent*. 2019;11(5):e482–e490.
50. Zhang X, Xu H, Zuo Z, Lin Z, Ferdov S, Dong J. Hydrothermal synthesis of copper zirconium phosphate hydrate $[Cu(OH)_2 Zr(HPO_4)_2{\cdot}2H_2O]$ and an investigation of its lubrication properties in grease. *ACS Appl Mater Interfaces*. 2013;5:7989–7994.
51. Cruz E, Broker EJ, Mosby BM. Combination of intercalation and surface modification in layered zirconium phosphates: investigation of surface stability and reactivity. *Dalton Trans*. 2020;49:3841–3848.
52. Cury SE, Aliaga-Del Castillo A, Pinzan A, et al. Orthodontic brackets friction changes after clinical use: a systematic review. *J Clin Exp Dent*. 2019;11(5):e482–e490.
53. Ma R, Sasaki T. Nanosheets of oxides and hydroxides: ultimate 2D charge-bearing functional crystallites. *Adv Mater*. 2010;22:5082–5104.
54. Zhao J, Huang Y, He Y, Shi Y. Nanolubricant additives: a review. *Friction*. 2021;9:891–917.
55. He X, Xiao H, Choi H, et al. α-zirconium phosphate nanoplatelets as lubricant additives. *Colloids Surf A Physicochem Eng Asp*. 2014;452:32–38.
56. Kalita H, Pal P, Dhara S, Pathak A. Fabrication and characterization of polyvinyl alcohol/metal (Ca, Mg, Ti) doped zirconium phosphate nanocomposite films for scaffold-guided tissue engineering application. *Mater Sci Eng C Mater Biol Appl*. 2017;71:363–371.
57. Zhang W, Qin P, Wang Z, et al. Superior wear resistance in EBM-processed TC4 alloy compared with SLM and forged samples. *Materials (Basel)*. 2019;12(5):782.
58. Wang S, Deng Y, Yang L, Shi X, Yang W, Chen ZG. Enhanced antibacterial property and osteo-differentiation activity on plasma treated porous polyetheretherketone with hierarchical micro/nano-topography. *J Biomater Sci Polym Ed*. 2018;29:520–542.
59. Ruan D, Wu C, Deng S, Zhang Y, Guan G. The anatase phase of nanotopography titania with higher roughness has better biocompatibility in osteoblast cell morphology and proliferation. *Biomed Res Int*. 2020;2020:8032718.